Stability and thermoelectric performance of the two-dimensional rare-earth compounds *R*TeCl (R = La, Pr, Nd)

Haoran Wei,[1] Xin Jin,[2] Xiaoliang Xiao,[1] Li Shi,[1] Yuanhao Duan,[1] Jing Fan,[3] Rui Wang,[1,4,5] and Xiaozhi Wu[1,5,*]

[1] *Institute for Structure and Function & Department of Physics, Chongqing University, Chongqing 400044, China*
[2] *College of Physics and Electronic Engineering, Chongqing Normal University, Chongqing 401331, China*
[3] *Center for Computational Science and Engineering, Southern University of Science and Technology, Shenzhen 518055, China*
[4] *Center of Quantum Materials and Devices, Chongqing University, Chongqing 400044, China*
[5] *Chongqing Key Laboratory for Strongly Coupled Physics, Chongqing 400044, China*

(Received 5 December 2023; revised 13 March 2024; accepted 16 April 2024; published 13 May 2024)

Thermoelectric conversion technology is increasingly important for sustainable energy, particularly in transforming waste heat into electricity. In this study, we explore the thermoelectric properties of three novel two-dimensional materials, monolayer *R*TeCl (with R = La, Pr, Nd), using density-functional theory and semiclassical Boltzmann transport theory. These materials are stable and can be easily exfoliated from bulk structures due to their low cleavage energy. Notably, monolayer *R*TeCl materials have high power factors ($(2.04–4.48) \times 10^4$ μW m^{-1} K^{-2}), attributed to multiple valleys in their valence-band maximum. Their complex crystal structures and the presence of two heavy elements contribute to an ultralow lattice thermal conductivity ((2.42–4.58) W m^{-1} K^{-1}) at room temperature. Impressively, the figure of merit (ZT) values of monolayer *R*TeCl range from 0.4 to 1.2 at 300 K. Across the temperature range of 300 to 700 K, the average ZT value and thermoelectric conversion efficiency reach 1.32–2.75 and 15.3%–22.6%, respectively. Our results indicate that monolayer *R*TeCl is a promising candidate for nanoelectronics and low-dimensional thermoelectric devices, offering a new avenue for high-performance thermoelectric materials.

DOI: 10.1103/PhysRevApplied.21.054026

I. INTRODUCTION

The rising anxiety around energy shortages and environmental degradation underscores the significance of advancing clean energy technologies and optimizing the recycling of current energy resources. Here, since thermoelectric materials can directly convert heat energy into electrical energy without causing environmental pollution, these materials exhibit significant promise, particularly in recycling industrial waste heat. For thermoelectric materials, one of the most important and most relevant features is the thermoelectric conversion efficiency η, which is typically quantified by the dimensionless figure of merit $ZT = \sigma S^2 T/(\kappa_e + \kappa_l)$ [1], where S, σ, T, κ_e, and κ_l denote the Seebeck coefficient, electrical conductivity, absolute temperature, electrical thermal conductivity, and lattice thermal conductivity, respectively. Based on the ZT value and the operating temperature range of the material, η can be roughly estimated by [2]

$$\eta = \frac{(T_h - T_c)}{T_h} \frac{(1 + ZT_{\text{avg}})^{1/2} - 1}{(1 + ZT_{\text{avg}})^{1/2} + T_c/T_h},$$

where ZT_{avg}, T_h, and T_c are the average ZT values across the temperature range, hot-end, and cold-end temperatures, respectively. One can see that a larger ZT value means a higher η.

Hence, in the realm of thermoelectric materials, achieving high performance usually necessitates the simultaneous optimization of two key factors, i.e., a higher power factor $F_P = \sigma S^2$ and a low thermal conductivity κ ($\kappa = \kappa_e + \kappa_l$). However, previous studies have indicated that a significant increase in F_P is challenging due to the strong coupling between the Seebeck coefficient and electrical conductivity [3]. In contrast, a substantial decrease in κ is comparatively more feasible. Various methods have been proven to be effective in reducing κ_l, including nanostructures [4], alloying [5], and searching for materials with lower intrinsic κ_l. Notably, some materials such as Ba_2BiAu [6], $MgIn_2Se_4$ [7], NaMgAs [8], bilayer

*Corresponding author: xiaozhiwu@cqu.edu.cn

SnSe [9], and tetradymites [10] have achieved high ZT values with ultralow κ_l.

Recently, two-dimensional (2D) materials have garnered significant research interest owing to their distinctive morphology and innovative physical properties. Besides, due to the size effect and the quantum confinement effect [11], 2D materials can exhibit lower κ_l, which endows them with considerable potential in thermoelectric device applications. With the development of 2D material preparative techniques, a series of 2D materials have been demonstrated as exceptional thermoelectric conversion properties, such as SnSe [12,13], MoS_2 [14], Bi_2Te_3 [4], black phosphorus [15], and Mo_2TiC_2 [16]. In general, materials with low intrinsic κ_l exhibit certain characteristics: (i) the presence of relatively heavy elements in the crystal; (ii) a crystal cell containing as many atoms as possible; and (iii) an exceedingly complex lattice structure. These particular attributes are responsible for the heightened occurrence of phonon scattering, leading to lower κ_l.

Various experimental and theoretical investigations have documented the existence of materials exhibiting these mentioned characteristics and ultralow κ_l, examples including 2D Ag_9AlSe_6 [17], $BaAg_2Te_2$ [18], Tl_3VSe_4 [19], and Cs_2SnBr_6 [20]. Moreover, numerous studies have demonstrated that tellurium-based compounds generally exhibit high S and low κ_l, resulting in large ZT values, as seen in PbTe [21], Bi_2Te_3 [22], Ag_2Te [23], and $CuGaTe_2$ [24]. Interestingly, ternary layered tellurides, such as $FeNbTe_2$ [25], $Cr_2Ge_2Te_6$ [26], and Nb_3SiTe_6 [27], which have recently been shown to have great potential in the field of voltage-controlled magnetoelectronics and topological states, have the characteristics above associated with them. Here, a crystal library, which reveals a series of ternary layered tellurides RTeCl with a suitable electronic structure (except that the band gap of CeTeCl is zero), has also been synthesized by Larres *et al.* [28]. These compounds represent the first example of rare-earth-metal telluride chlorides. They contain two heavy elements, and their monolayers consist of multiple atomic layers. Therefore, it could be expected that their κ_l values are relatively small.

In this work, the stabilities and thermoelectric properties of the monolayer RTeCl have been studied systematically. The low cleavage energy and the high thermodynamic and kinetic stabilities guarantee the possibility of experimental synthesis of monolayer RTeCl. Furthermore, owing to their unique atomic arrangement and the inclusion of two heavy-element components, the three monolayers demonstrate a remarkable S value of $(1\text{–}1.5) \times 10^3$ μV K^{-1} and significantly low κ_l ((2.42–4.58) W m^{-1} K^{-1}). Accordingly, their power factors F_P reach $(2.04\text{–}4.48) \times 10^4$ μW m^{-1} K^{-2} and ZT values are up to 0.93, 1.06, and 1.2 at room temperature. This exceptional performance endows 2D RTeCl with substantial application prospects in the realm of thermoelectricity.

II. COMPUTATIONAL METHODS

All calculations were performed using the projector augmented-wave method in the Vienna *Ab initio* Simulation Package (VASP) [29,30]. The plane-wave cutoff energy was set to 520 eV. The Perdew-Burke-Ernzerhof (PBE) version of the generalized gradient approximation (GGA) was utilized to account for the exchange-correlation energy [31]. For the structural optimization, the energy convergence threshold between two consecutive parts was set to 10^{-8} eV, and the Hellman-Feynman force convergence threshold was set to 10^{-3} eV Å^{-1}. The first Brillouin zone (BZ) is sampled by using an $11 \times 11 \times 1$ Γ-centered **k** mesh. To avoid interlayer interactions caused by periodic boundary conditions, a 15 Å vacuum layer was set vertically. In addition, considering that GGA usually underestimates the band gap of semiconductors, the hybrid functional HSE06 was further used to calculate the electronic band structure [32].

The spin-orbit coupling (SOC) effect was also considered in electronic-structure calculations due to the presence of the two heavier elements in the monolayer RTeCl [33]. To evaluate the thermal stability of monolayer RTeCl, *ab initio* molecular dynamics (AIMD) simulations were performed in a canonical ensemble using the Verlet algorithm. A 10 ps AIMD simulation was performed with a $5 \times 5 \times 1$ supercell at 700 K [34]. The phonon dispersion and thermal transport parameters with a $4 \times 4 \times 1$ supercell were determined using the PHONOPY and PHONO3PY software packages, respectively [35,36]. The HIPHIVE code, which utilizes machine learning techniques, was employed to extract higher-order mechanical constants [37,38]. This approach has demonstrated its efficacy in precisely assessing the κ_l values of many commonly encountered 2D materials [39]. We chose the effective thicknesses (10.84, 10.88, and 10.85 Å) of monolayer RTeCl as the thicknesses in the κ_l calculation. The WANNIER90 code and its accompanying Boltzmann transport module were employed for the investigation of electrical transport characteristics [40].

III. RESULTS AND DISCUSSION

A. Crystal structure and stability

The synthesis of 2D materials has consistently been a focal point of research at the forefront of scientific investigation. At present, mechanical stripping of monolayers from layered bulk materials is the dominant experimental technique for producing 2D materials, with well-known examples including graphene, SnSe, Bi_2Te_3, and MoS_2. Intriguingly, bulk RTeCl, a layered material yet to be extensively explored, depicted in Fig. 1(a), was first synthesized by Larres *et al.* [28]. Bulk RTeCl is a tetragonal lattice and belongs to space group $P4/nmm$ (No. 129). Owing to its D_{4h} symmetry, monolayer RTeCl displays identical characteristics in both the a and b directions

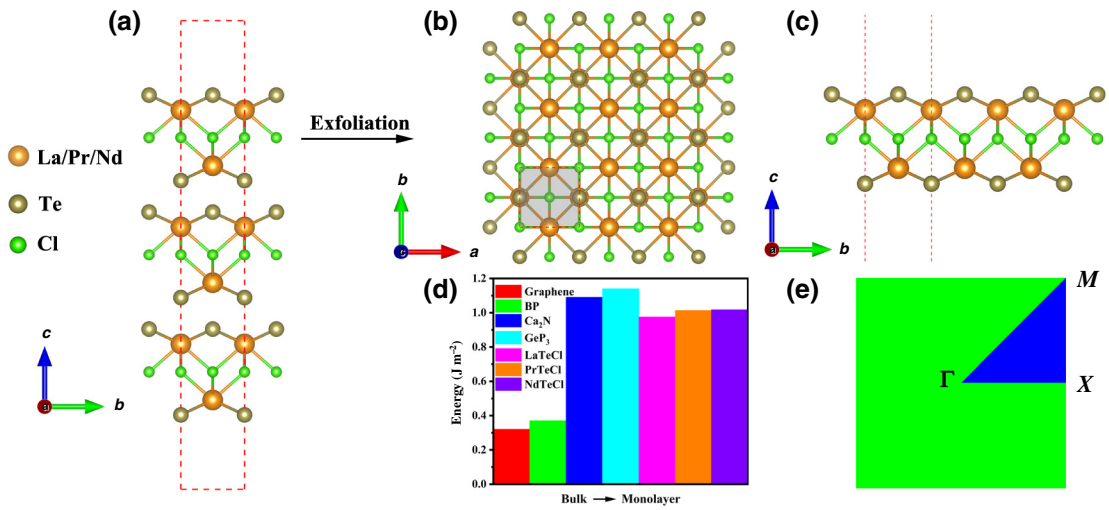

FIG. 1. (a) Side view of the structure of bulk crystalline *R*TeCl. (b) Top and (c) side views of corresponding monolayer *R*TeCl. (d) Cleavage energies of monolayer *R*TeCl. (e) The 2D Brillouin zone with high-symmetry paths.

[Figs. 1(b) and 1(c)]. The lattice parameters are included in Table I. Consequently, the following computations only focus on one of the directions.

To assess the possibility of mechanical exfoliation of the *R*TeCl monolayer, we calculate the cleavage energies of three monolayers using the rigorous method [41], $E_f = (E_{\rm iso} - E_{\rm bulk}/n)/\mathcal{A}$, where $E_{\rm iso}$ and $E_{\rm bulk}$ are the energies of the monolayer and the bulk, and n and $\mathcal{A}$ are the number of layers and the in-plane area of the unit cell, respectively. As illustrated in Fig. 1(c) and Table I, the calculated cleavage energies are 0.98, 1.01, and 1.02 J m^{-2}, respectively, which are slightly higher than those for graphene (0.33 J m^{-2}) [42], MoS_2 (0.27 J m^{-2}) [43], and phosphorus (0.36 J m^{-2}) [44] but lower than that for GeP_3 (1.14 J m^{-2}) [45], suggesting that mechanical exfoliation would be highly experimentally practicable.

According to many previous reports on 2D materials, freestanding 2D materials not only need to be easily prepared by mechanical exfoliation but also need to have thermodynamic, kinetic, and mechanical stability [46–49]. Firstly, we evaluate the thermodynamic stability via AIMD simulations, as shown in Fig. S1 in the Supplemental Material [50]. The monolayers exhibit negligible structural reconfiguration and minor total energy fluctuations after a 10-ps simulation at 700 K, indicating robust thermodynamic stability. Subsequently, phonon dispersions are employed to assess kinetic stability. As depicted in Figs. 2(a)–2(c), the absence of imaginary frequencies across the BZ confirms the dynamic stability of these phases. In addition, the mechanical stability is evaluated by calculating the elastic constants, as listed in Table II. All three monolayers satisfy the Born-Huang criteria [51]: $C_{11}C_{22} - C_{12}^2 > 0$ and $C_{66} > 0$. On this basis, since these three materials are tetragonal crystals, we introduce a more accurate mechanical stability criterion based on their point-group ($4/mmm$) characteristics [52]: $C_{11} > |C_{12}|$ and $2C_{13}^2 < C_{33}(C_{11} + C_{12})$. They also satisfy this criterion, illustrating their high mechanical stability. The above results imply that these 2D materials are amenable to experimental synthesis.

Furthermore, due to the D_{4h} symmetry, we obtain the in-plane Young's modulus $Y(\theta)$ and Poisson's ratio $\nu(\theta)$ in the following forms in polar coordinates [53,54]:

$$Y(\theta) = \frac{\Delta C}{C_{11}(\alpha^4 + \beta^4) + (\Delta C/C_{66} - 2C_{12})\alpha^2\beta^2}, \quad (1)$$

$$\nu(\theta) = -\frac{(2C_{11} - \Delta C/C_{66})\alpha^2\beta^2 - C_{12}(\alpha^4 + \beta^4)}{C_{11}(\alpha^4 + \beta^4) + (\Delta C/C_{66} - 2C_{12})\alpha^2\beta^2}, \quad (2)$$

TABLE I. Lattice parameter a (Å), cleavage energies (J m^{-2}), and different functional (PBE and HSE06) band gaps (eV) considering SOC for the monolayer *R*TeCl.

			Band gap	
Monolayer	a	E_f	PBE	HSE06
LaTeCl	4.39	0.98	0.91	1.53
PrTeCl	4.34	1.01	0.73	1.37
NdTeCl	4.31	1.02	0.72	1.34

TABLE II. Elastic constants C_{ij} (N m^{-1}), maximum Young's moduli $Y_{\rm max}$ (N m^{-1}), and maximum Poisson's ratios $\nu_{\rm max}$.

Monolayer	C_{11}	C_{12}	C_{66}	$Y_{\rm max}$	$\nu_{\rm max}$
LaTeCl	78.50	37.95	32.80	60.15	0.48
PrTeCl	80.77	41.99	34.58	58.95	0.52
NdTeCl	81.41	44.53	35.26	57.06	0.55

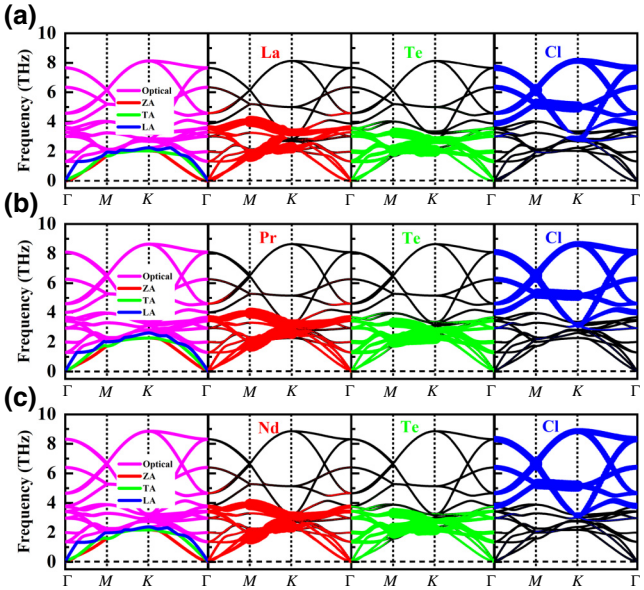

FIG. 2. The orbital-resolved phonon dispersion of monolayer *R*TeCl, for *R* = La (a), Pr (b), and Nd (c).

where $C_{11} = C_{22}$, $\Delta C = C_{11}^2 - C_{12}^2$, $\alpha = \cos(\theta)$, and $\beta = \sin(\theta)$, with angle θ being with respect to the a axis. As displayed in Fig. S2 in the Supplemental Material [50], it is obvious that Young's modulus and Poisson's ratio show D_{4h} symmetry, which is consistent with their crystal symmetry. The calculated maximum Young's moduli $Y_{\max}$ are 60.15, 58.95, and 57.06 N m^{-1}, respectively, while the corresponding maximum Poisson's ratios $\nu_{\max}$ are 0.48, 0.52, and 0.55 (see Table II). The relatively low Young's moduli and high Poisson's ratios indicate the excellent flexibility of the monolayer *R*TeCl, widening their potential scope for applications. The aforementioned findings demonstrate that the mechanical stripping method yields 2D *R*TeCl materials with exceptional stability.

B. Electronic structure and transport properties

The electrical transport properties of monolayer *R*TeCl are determined by its electronic structure. Firstly, we carefully tested the magnetic properties by both high-precision structure optimization and self-consistent calculations. Then, we also tested the magnetic moments with different Hubbard-Coulomb interaction U values. These calculated results all consistently displayed magnetic moments of zero for the three materials, suggesting that they are nonmagnetic systems. Finally, with consideration of SOC, we tested the different magnetic directions and magnetic configurations, which also basically yielded zero-magnetic-moment results in the different directions. Besides, as it arises from two heavy atoms (*R* and Te), the SOC effect has a significant impact on both the band gap and band dispersion, as depicted in Fig. S3 in the

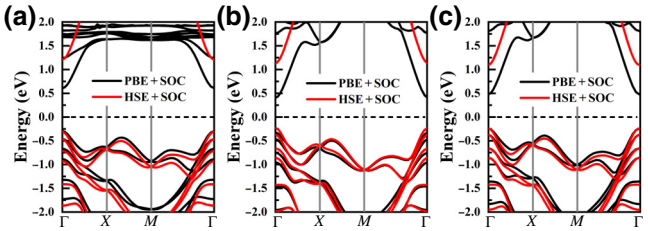

FIG. 3. The PBE and HSE06 electronic band structures of monolayer *R*TeCl, for *R* = La (a), Pr (b), and Nd (c), with SOC.

Supplemental Material [50]. Therefore, in the subsequent calculations, we mainly focus on the results with SOC.

As is well known, since the PBE method typically underestimates the band gap of semiconductor materials, we conduct calculations using both the PBE and HSE06 approaches, as illustrated in Figs. 3(a)–3(c). They all exhibit a direct band gap with the valence-band maximum (VBM) and the conduction-band minimum (CBM) located at the Γ point. Their band gaps are 1.53, 1.37, and 1.34 eV under the HSE06 approach (0.91, 0.73, and 0.72 eV with the PBE scheme), respectively. Here, it is worth noting that their CBMs are steeper, while the VBMs possess multivalley characteristics and undergo simplification, indicating that the monolayer *R*TeCl exhibits a high carrier mobility and a significant effective-mass density of states (DOS). This predicts that monolayer *R*TeCl will possess a high conductance with a large σ, enabling decoupling to some extent. The projected density of states is shown in Fig. S4 in the Supplemental Material [50]. The results indicate that the VBMs are primarily contributed from p orbitals of Te, while the CBMs are mainly derived from d orbitals of the rare-earth elements (La, Pr, and Nd).

In addition, we calculated the electronic band structures of the bulk forms of these three materials, as shown in Figs. S5(a)–S5(c) in the Supplemental Material [50]. The band structure of the bulk is very similar to that of the monolayer and shows a direct band gap, but the band gap is smaller.

To facilitate a more comprehensive investigation of the electronic properties, we utilize deformation potential theory (DPT) to assess its effective mass and carrier mobility [55]:

$$\mu_{2D} = \frac{2e\hbar^3 C_{2D}}{3k_B T|m^*|^2 (E_l^i)^2}. \tag{3}$$

Here μ_{2D}, $\hbar$, k_B, and T represent the carrier mobility, reduced Planck's constant, Boltzmann constant, and temperature, respectively; C_{2D} is the plane stiffness; and E_l^i represents the deformation potential constant, $E_l^i = \Delta E_i/\xi$, where ΔE_i denotes the energy changes of the ith band at small strains and ξ denotes the degree of strain, $\xi = \Delta l/l_0$ (where l_0 is the lattice constant in the transport direction and Δl is the deformation of l_0). Finally, m^*

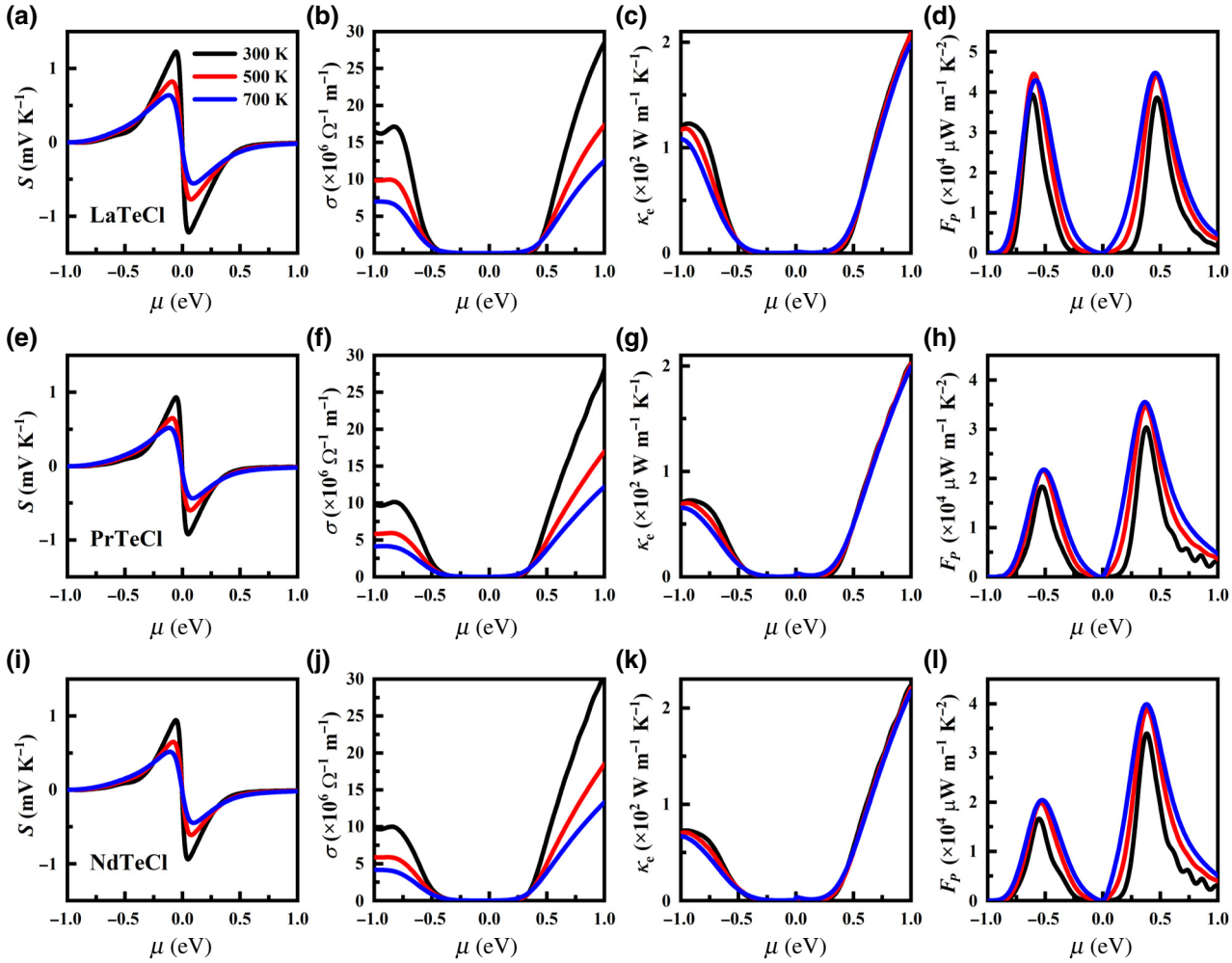

FIG. 4. Electron transport properties of monolayer RTeCl, for R = La (top row), Pr (middle row), and Nd (bottom row): (a),(e),(i) Seebeck coefficients S, (b),(f),(j) electrical conductivities σ, (c),(g),(k) electron thermal conductivities κ_e, and (d),(h),(l) power factors F_P, all at 300, 500, and 700 K.

represents the carrier effective mass and is expressed as $m^* = \hbar^2/(\partial^2 E/\partial^2 k)$, where E and k are the energy and wave vector [56]. The results are shown in Table S1 in the Supplemental Material [50]. Monolayer RTeCl features a small electronic effective mass (0.36–0.37), leading to very high electronic mobility μ^e_{2D}, which is consistent with the steep dispersion distribution of the CBM.

The aforementioned electronic characteristics collectively illustrate the exceptional electrical transport properties. Furthermore, we have derived a set of transport properties by solving the Boltzmann transport equation, including S, σ, κ_e, and F_P, as shown in Figs. 4(a)–4(l). First of all, the Seebeck coefficient can be expressed as

$$S = \frac{8\pi^2 k_B^2 T m_d^*}{3e\hbar^2}\left(\frac{\pi}{3n}\right)^{2/3}, \tag{4}$$

where m_d^* and n represent the DOS effective mass and the carrier concentration, respectively [57]. The value of S is obviously proportional to m_d^*. The multivalley energy-band feature at the VBM leads to a better distribution of the DOS effective mass, which is shown by the remarkably steep DOS distribution at the VBM. With a sharper DOS distribution at the band edge, a higher S can be achieved. As predicted, the three monolayers demonstrate large S values ((1–1.5) $\times 10^3$ μV K^{-1}) at room temperature, which are larger than those of some of the high-performance thermoelectric materials, such as functionalized monolayer Sc_2C (372–1036 μV K^{-1}), Cu_2S (250–300 μV K^{-1}), and M_2CO_2 (M = Ti, Zr, and Hf) (1100 μV K^{-1}).

According to Eq. (S1) in the Supplemental Material [50], the σ and κ_e values are directly related to the carrier relaxation time τ. Hence, we calculated τ using the currently common DPT for different temperatures and different carrier types [58]: $\tau = m^*\mu/e$. The results are shown in Table S1 in the Supplemental Material [50]. The relaxation times of electrons and holes at 300 K are (22.2–52.1) $\times 10^{-14}$ and (3.2–14.2) $\times 10^{-14}$ s,

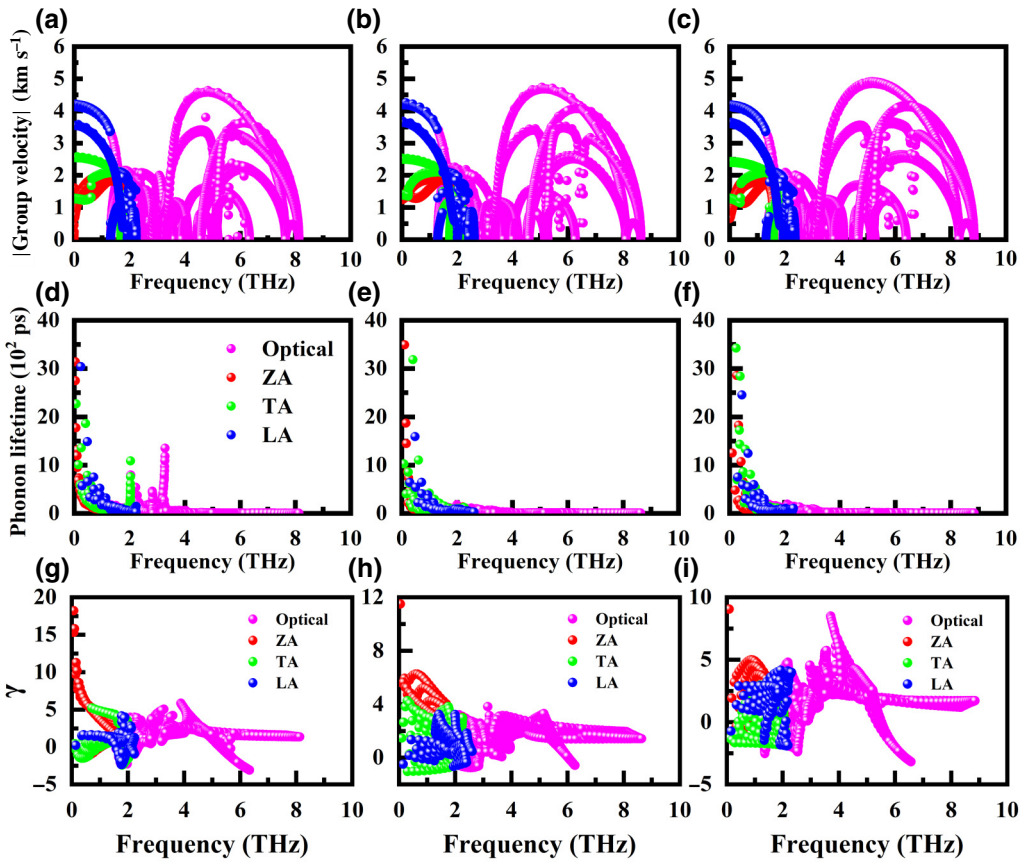

FIG. 5. (a)–(c) Group velocities, (d)–(f) phonon lifetimes, and (g)–(i) Grüneisen parameters of monolayer *R*TeCl, for *R* = La (left column), Pr (middle column), and Nd (right column), where the red, green, blue, and pink dots correspond to ZA, TA, LA, and optical phonons, respectively.

respectively. Additionally, for the semiconductors, higher carrier mobility μ also tends to result in higher σ [59], i.e., $\sigma = n\mu e$. The σ values of monolayer *R*TeCl are as high as (10^6–10^7) Ω^{-1} m^{-1}. The F_P values also reach (2.04–4.48) $\times$ 10^4 μW m^{-1} K^{-2}, which is comparable to those of some excellent thermoelectric materials, such as PbTe ($\sim$2.0 $\times$ 10^3 μW m^{-1} K^{-2}) [22] and Bi_2Te_3 ($\sim$4.5 $\times$ 10^3 μW m^{-1} K^{-2}) [11].

C. Phonon thermal transport

Upon predicting the exceptional electrical transport properties, we further evaluated the thermal transport properties of these monolayers. Here, the three lowest acoustic modes are the out-of-plane acoustic branch (ZA), the transverse acoustic branch (TA), and the longitudinal acoustic branch (LA), respectively [see Figs. 2(a)–2(c)]. Macroscopically, the acoustic and low-frequency optical modes are contributed by the heavier rare-earth elements *R* (La, Pr, and Nd) and Te, whereas the lighter element Cl contributes to the high-frequency optical modes. Owing to the two heavier elements, the phonon vibrational frequencies are notably low, with a maximum frequency of merely 8–9 THz, suggesting a potential for low κ_l. Here, κ_l can be expressed as $\kappa_l = \sum_\lambda c_{\mathrm{ph}\lambda} v_{\alpha\lambda}^2 \tau_\lambda$, where $c_{\mathrm{ph}\lambda}$, $v_{\alpha\lambda}$, and τ_λ are the volumetric specific heat, phonon group velocity, and phonon lifetime, respectively; and λ denotes the λth branch of phonon mode [60]. The absence of a phononic gap between the acoustic and optical modes makes it easier for phonons to scatter between them. At the same time, the coupling between the low-frequency optical mode and LA, as well as ZA and TA along the Γ-M direction, which also provides more scattering channels for optical and acoustic phonons, further enhances the phonon scattering and reduces the phonon lifetime τ_λ, as shown in Figs. 5(d)–5(f). The distribution of phonon lifetimes suggests that the main contribution to κ_l comes from the acoustic modes, and there is a smaller contribution from the optical mode.

Besides, κ_l is highly correlated with the phonon group velocity, i.e., $\kappa_l \propto v_{\alpha\lambda}^2$. The group velocity of acoustic modes is mainly distributed below 4.5 km s^{-1} [see Figs. 5(a)–5(c)], which is much lower than that of graphene ($\sim$22 km s^{-1}) [61], and comparable to those of arsenene ($\sim$4.5 km s^{-1}) [62], $Rb_2B_3C_4$ (4 km s^{-1}) [40], and $MoSe_2$ ($\sim$5.06 km s^{-1}) [63]. The maximum group

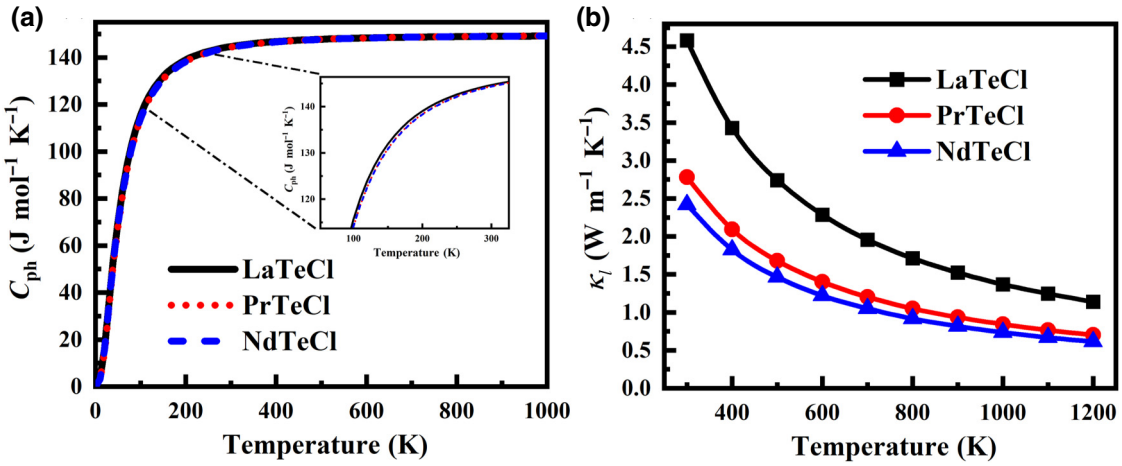

FIG. 6. (a) Volumetric specific heat and (b) lattice thermal conductivity of monolayer RTeCl, for R = La, Pr, and Nd.

velocity of the optical mode can reach 5 km s^{-1}, which corresponds to a steep phonon dispersion in the range of 4–9 THz.

Meanwhile, the distribution of volumetric heat capacity is about 145 J mol^{-1} K^{-1}, as shown in Fig. 6(a), and the volumetric heat capacities of three monolayers are very close due to their similar structures and chemical compositions. Furthermore, we calculate the Grüneisen parameter (γ), which represents the phonon-phonon anharmonicity and can be expressed as $\gamma = (V/\omega(q))\,\partial\omega(q)/\partial V$ [64], where V and $\omega(q)$ denote the crystal volume and phonon frequency, respectively. In general, a large $|\gamma|$ indicates strong phonon-phonon anharmonic scattering [65]. As shown in Figs. 5(g)–5(i), the monolayer RTeCl has a larger γ and poorer convergence, compared to other conventional 2D materials [66,67]. This means that monolayer RTeCl has strong phonon-phonon anharmonic scattering, resulting in the low τ_λ and κ_l.

The intrinsic κ_l is shown in Fig. 6(b). These monolayers exhibit extremely low κ_l values of 4.58, 2.78, and 2.42 W m^{-1} K^{-1} at 300 K, which are comparable to those of excellent thermoelectric materials, such as antimonene (5 W m^{-1} K^{-1}) [62], Bi_2Te_3 (~2.5 W m^{-1} K^{-1}) [68], PbTe (2.01 W m^{-1} K^{-1}) [69], and monolayer SnSe ((2.02–2.5) W m^{-1} K^{-1}) [70]. Here, one can see that κ_l decreases as the temperature increases, indicating that Umklapp phonon scattering plays a dominant role. Besides, as the three rare-earth elements (La, Pr, and Nd) gradually become heavier, phonon scattering also becomes stronger, giving rise to a gradually decreasing κ_l value.

D. Thermoelectric figure of merit *ZT*

The ZT values at different temperatures (300, 500, and 700 K) can be determined from electrical and thermal transport parameters, as illustrated in Figs. 7(a)–7(c). It is evident that the ZT values of n-type doping are significantly superior to those of p-type doping. At 300 K, the ZT values range from 0.4 to 1.2, comparable to those for other 2D materials, such as InSe (0.5) [71] and PbTe (0.3) [22]. As the temperature rises, the ZT values increase significantly and the accompanying peaks shift toward the region of low chemical potential. At 700 K, the ZT values increase to 2.34–4.15, exceeding those of GaTe (0.7) [72], PbTe (1.2) [22], and $MgIn_2Se_4$ (3.06) [7]. The ZT values of monolayer RTeCl (R = La, Pr, and Nd) as a function of carrier concentration are shown in Fig. S6 in the Supplemental Material [50]. The results indicate that the ZT peaks of the three materials are in the range of carrier concentration of 10^{12}–10^{13} cm^{-2}, which is a feasible range attainable in experiments.

In addition, we calculate the average ZT values (ZT_{avg}) and conversion efficiency η in the temperature range of 300–700 K, as shown in Table SI in the Supplemental Material [50]. Their average ZT and η values reach 1.32–1.59 and 15.3%–17.1% for p-type doping and 2.28–2.75 and 20.7%–22.6% for n-type doping. Collectively, monolayer RTeCl is expected to have great potential in nanoelectronic materials and low-dimensional thermoelectrics.

IV. SUMMARY

In summary, we have theoretically predicted three monolayer semiconductor materials with two heavy elements. The low cleavage energies (0.98–1.02 J m^{-2}) validate the feasibility of mechanically exfoliating the three monolayers from their bulk structures. The kinetic, thermodynamic, and mechanical stabilities of monolayer RTeCl are confirmed by phonon dispersion, AIMD simulations, and elastic constant constraints, respectively. The three monolayers show direct-band-gap features with values of 1.53, 1.37, and 1.34 eV, respectively. In addition, they exhibit a high F_P ((2.04–4.48) $\times$ 10^4 μW m^{-1} K^{-2})

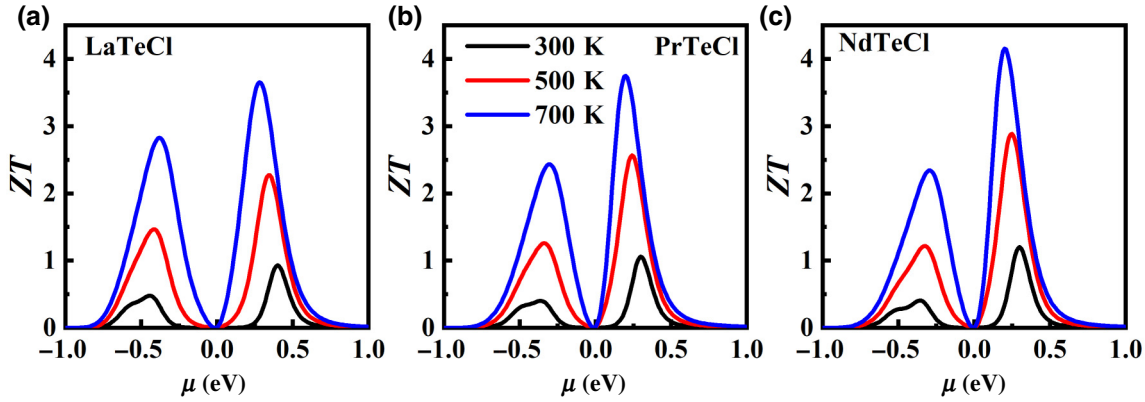

FIG. 7. The *ZT* values of monolayer *R*TeCl, for *R* = La (a), Pr (b), and Nd (c), at 300, 500, and 700 K.

and an ultralow κ_l ((2.42–4.58) W m^{-1} K^{-1}), leading to high *ZT* values (0.4–1.2) at room temperature as well as an η value of approximately 22.6% within the temperature range of 300–700 K. Our findings suggest that *R*TeCl monolayers are promising candidates for advanced thermoelectric applications in nanoelectronics and innovative thermoelectric devices.

ACKNOWLEDGMENTS

This work was supported by the Natural Science Foundation of China (NSFC, Grants No. 12174040, No. 12204074, No. 12222402, No. 11974062, and No. 12147102) and by the Chongqing Natural Science Foundation (Grant No. cstc2020jcyj-msxmX0118).

[1] L.-D. Zhao, G. Tan, S. Hao, J. He, Y. Pei, H. Chi, H. Wang, S. Gong, H. Xu, V. P. Dravid, C. Uher, G. J. Snyder, C. Wolverton, and M. G. Kanatzidis, Ultrahigh power factor and thermoelectric performance in hole-doped single-crystal SnSe, Science **351**, 141 (2016).

[2] V. Dusastre, *Materials for Sustainable Energy: A Collection of Peer-Reviewed Research and Review Articles from Nature Publishing Group* (World Scientific, London, 2010).

[3] T. Yue, Y. Zhao, J. Ni, S. Meng, and Z. Dai, Strong quartic anharmonicity, ultralow thermal conductivity, high band degeneracy and good thermoelectric performance in Na_2TlSb, npj Comput. Mater. **9**, 17 (2023).

[4] M. Hong, T. C. Chasapis, Z.-G. Chen, L. Yang, M. G. Kanatzidis, G. J. Snyder, and J. Zou, n-Type $Bi_2Te_{3-x}Se_x$ nanoplates with enhanced thermoelectric efficiency driven by wide-frequency phonon scatterings and synergistic carrier scatterings, ACS Nano **10**, 4719 (2016).

[5] Z. Chen, B. Gao, J. Tang, X. Guo, W. Li, and R. Ang, Low lattice thermal conductivity by alloying SnTe with $AgSbTe_2$ and CaTe/MnTe, Appl. Phys. Lett. **115**, 073903 (2019).

[6] J. Park, Y. Xia, and V. Ozoliņš, High thermoelectric power factor and efficiency from a highly dispersive band in Ba_2BiAu, Phys. Rev. Appl. **11**, 014058 (2019).

[7] W. Fang, K. Kuang, X. Xiao, H. Wei, Y. Chen, M. Li, and Y. He, Ab initio study of two-dimensional $MgAl_2Se_4$ and $MgIn_2Se_4$ with high stability, high electron mobility, and high thermoelectric figure of merit, J. Alloys Compd. **931**, 167586 (2023).

[8] J.-H. Yuan, Y.-L. Zhu, W.-Y. Fang, S.-X. Yang, K.-H. Xue, N. Bai, L. Ye, X. Cheng, and X. Miao, Two-dimensional *A*Mg*B* (*A* = Na, K; *B* = P, As, Sb, Bi) with promising optoelectronic and thermoelectric performances, ACS Appl. Electron. Mater. **5**, 1405 (2023).

[9] S. Nag, A. Saini, R. Singh, and R. Kumar, Ultralow lattice thermal conductivity and anisotropic thermoelectric performance of AA stacked SnSe bilayer, Appl. Surf. Sci. **512**, 145640 (2020).

[10] N. T. Hung, A. R. Nugraha, and R. Saito, Designing high-performance thermoelectrics in two-dimensional tetradymites, Nano Energy **58**, 743 (2019).

[11] L. D. Hicks and M. S. Dresselhaus, Effect of quantum-well structures on the thermoelectric figure of merit, Phys. Rev. B **47**, 12727 (1993).

[12] L.-D. Zhao, S.-H. Lo, Y. Zhang, H. Sun, G. Tan, C. Uher, C. Wolverton, V. P. Dravid, and M. G. Kanatzidis, Ultralow thermal conductivity and high thermoelectric figure of merit in SnSe crystals, Nature **508**, 373 (2014).

[13] C. Chang, M. Wu, D. He, Y. Pei, C.-F. Wu, X. Wu, H. Yu, F. Zhu, K. Wang, Y. Chen, L. Huang, J.-F. Li, J. He, and L.-D. Zhao, 3D charge and 2D phonon transports leading to high out-of-plane *ZT* in n-type SnSe crystals, Science **360**, 778 (2018).

[14] J. Wu, H. Schmidt, K. K. Amara, X. Xu, G. Eda, and B. Özyilmaz, Large thermoelectricity via variable range hopping in chemical vapor deposition grown single-layer MoS_2, Nano Lett. **14**, 2730 (2014).

[15] C. J. An, Y. H. Kang, C. Lee, and S. Y. Cho, Preparation of highly stable black phosphorus by gold decoration for high-performance thermoelectric generators, Adv. Funct. Mater. **28**, 1800532 (2018).

[16] H. Kim, B. Anasori, Y. Gogotsi, and H. N. Alshareef, Thermoelectric properties of two-dimensional molybdenum-based MXenes, Chem. Mater. **29**, 6472 (2017).

[17] W. Li, S. Lin, M. Weiss, Z. Chen, J. Li, Y. Xu, W. G. Zeier, and Y. Pei, Crystal structure induced ultralow lattice

thermal conductivity in thermoelectric Ag_9AlSe_6, Adv. Energy Mater. **8**, 1800030 (2018).

[18] J. Tang, C. Qin, H. Yu, Z. Zeng, L. Cheng, B. Ge, Y. Chen, W. Li, and Y. Pei, Ultralow lattice thermal conductivity enables high thermoelectric performance in $BaAg_2Te_2$ alloys, Mater. Today Phys. **22**, 100591 (2022).

[19] Y. Xia, K. Pal, J. He, V. Ozoliņš, and C. Wolverton, Particlelike Phonon Propagation Dominates Ultralow Lattice Thermal Conductivity in Crystalline Tl_3VSe_4, Phys. Rev. Lett. **124**, 065901 (2020).

[20] X. Zeng, J. Jiang, G. Niu, L. Sui, Y. Zhang, X. Wang, X. Liu, A. Chen, M. Jin, and K. Yuan, Physical insights on the thermoelectric performance of Cs_2SnBr_6 with ultralow lattice thermal conductivity, J. Phys. Chem. Lett. **13**, 9736 (2022).

[21] Q. Zhang, S. Yang, Q. Zhang, S. Chen, W. Liu, H. Wang, Z. Tian, D. Broido, G. Chen, and Z. Ren, Effect of aluminum on the thermoelectric properties of nanostructured PbTe, Nanotechnology **24**, 345705 (2013).

[22] M. Scheele, N. Oeschler, K. Meier, A. Kornowski, C. Klinke, and H. Weller, Synthesis and thermoelectric characterization of Bi_2Te_3 nanoparticles, Adv. Funct. Mater. **19**, 3476 (2009).

[23] P. F. Taylor and C. Wood, Thermoelectric properties of Ag_2Te, J. Appl. Phys. **32**, 1 (2004).

[24] T. Plirdpring, K. Kurosaki, A. Kosuga, T. Day, S. Firdosy, V. Ravi, G. J. Snyder, A. Harnwunggmoung, T. Sugahara, Y. Ohishi, H. Muta, and S. Yamanaka, Chalcopyrite $CuGaTe_2$: A high-efficiency bulk thermoelectric material, Adv. Mater. **24**, 3622 (2012).

[25] W. Bai, Z. Hu, S. Wang, Y. Hua, Z. Sun, C. Xiao, and Y. Xie, Intrinsic negative magnetoresistance in van der Waals $FeNbTe_2$ single crystals, Adv. Mater. **31**, 1900246 (2019).

[26] C. Gong, L. Li, Z. Li, H. Ji, A. Stern, Y. Xia, T. Cao, W. Bao, C. Wang, Y. Wang, Z. Q. Qiu, R. J. Cava, S. G. Louie, J. Xia, and X. Zhang, Discovery of intrinsic ferromagnetism in two-dimensional van der Waals crystals, Nature **546**, 265 (2017).

[27] L. An, H. Zhang, J. Hu, X. Zhu, W. Gao, J. Zhang, C. Xi, W. Ning, Z. Mao, and M. Tian, Magnetoresistance and Shubnikov–de Haas oscillations in layered Nb_3SiTe_6 thin flakes, Phys. Rev. B **97**, 235133 (2018).

[28] M. Larres, I. Pantenburg, and G. Meyer, The first rare-earth metal telluride chlorides, RTeCl (R = La, Ce, Pr, Nd), Z. Anorg. Allg. Chem. **639**, 2744 (2013).

[29] J. Hafner, Ab-initio simulations of materials using VASP: Density-functional theory and beyond, J. Comput. Chem. **29**, 2044 (2008).

[30] P. E. Blöchl, Projector augmented-wave method, Phys. Rev. B **50**, 17953 (1994).

[31] J. P. Perdew, K. Burke, and M. Ernzerhof, Generalized Gradient Approximation Made Simple, Phys. Rev. Lett. **77**, 3865 (1996).

[32] J. Heyd, G. E. Scuseria, and M. Ernzerhof, Hybrid functionals based on a screened Coulomb potential, J. Chem. Phys. **118**, 8207 (2003).

[33] M. Filatov and D. Cremer, Calculation of indirect nuclear spin-spin coupling constants within the regular approximation for relativistic effects, J. Chem. Phys. **120**, 11407 (2004).

[34] G. Kresse and J. Hafner, Ab initio molecular dynamics for liquid metals, Phys. Rev. B **47**, 558 (1993).

[35] A. Togo, First-principles phonon calculations with Phonopy and Phono3py, J. Phys. Soc. Jpn. **92**, 012001 (2023).

[36] A. Togo and I. Tanaka, First principles phonon calculations in materials science, Scr. Mater. **108**, 1 (2015).

[37] F. Eriksson, E. Fransson, and P. Erhart, The Hiphive package for the extraction of high-order force constants by machine learning, Adv. Theor. Simul. **2**, 1800184 (2019).

[38] F. Pedregosa, G. Varoquaux, A. Gramfort, V. Michel, B. Thirion, O. Grisel, M. Blondel, P. Prettenhofer, R. Weiss, V. Dubourg, *et al.*, Scikit-learn: Machine learning in Python, J. Mach. Learn. Res. **12**, 2825 (2011).

[39] Y. Zhu, J.-H. Yuan, W.-Y. Fang, Z.-G. Sun, and J. Wang, A family of two-dimensional semiconductors with transition metal kagome lattice, large power factor and ultralow lattice thermal conductivity, Appl. Surf. Sci. **636**, 157817 (2023).

[40] G. Pizzi, *et al.*, Wannier90 as a community code: New features and applications, J. Phys.: Condens. Matter **32**, 165902 (2020).

[41] J. H. Jung, C.-H. Park, and J. Ihm, A rigorous method of calculating exfoliation energies from first principles, Nano Lett. **18**, 2759 (2018).

[42] Y.-Q. Song, J.-H. Yuan, L.-H. Li, M. Xu, J.-F. Wang, K.-H. Xue, and X.-S. Miao, KTlO: A metal shrouded 2D semiconductor with high carrier mobility and tunable magnetism, Nanoscale **11**, 1131 (2019).

[43] G. Levita, P. Restuccia, and M. Righi, Graphene and MoS_2 interacting with water: A comparison by ab initio calculations, Carbon **107**, 878 (2016).

[44] J.-H. Yuan, K.-H. Xue, J.-F. Wang, and X.-S. Miao, Gallium thiophosphate: An emerging bidirectional auxetic two-dimensional crystal with wide direct band gap, J. Phys. Chem. Lett. **10**, 4455 (2019).

[45] Y. Jing, Y. Ma, Y. Li, and T. Heine, GeP_3: A small indirect band gap 2D crystal with high carrier mobility and strong interlayer quantum confinement, Nano Lett. **17**, 1833 (2017).

[46] Y. Huang, E. Sutter, N. N. Shi, J. Zheng, T. Yang, D. Englund, H.-J. Gao, and P. Sutter, Reliable exfoliation of large-area high-quality flakes of graphene and other two-dimensional materials, ACS Nano **9**, 10612 (2015).

[47] S. Zhang, H. Wu, L. Yang, G. Zhang, Y. Xie, L. Zhang, W. Zhang, and H. Chang, Two-dimensional magnetic atomic crystals, Mater. Horiz. **9**, 559 (2022).

[48] Z. Xiao, R. Wang, D. Jiang, Z. Qian, Y. Li, K. Yang, Y. Sun, Z. Zeng, and F. Wu, Recent developments of two-dimensional anode materials and their composites in lithium-ion batteries, ACS Appl. Energy Mater. **4**, 7440 (2021).

[49] X. Mu, J. Wang, and M. Sun, Two-dimensional black phosphorus: Physical properties and applications, Mater. Today Phys. **8**, 92 (2019).

[50] See the Supplemental Material http://link.aps.org/supplemental/10.1103/PhysRevApplied.21.054026 for the AIMD simulation, $Y(\theta)$, $\nu(\theta)$, band dispersions with and without

SOC, DOS, C_{2D}, E_l^i, m^*, μ_{2D}, τ, ZT_{avg}, and η of monolayer *R*TeCl, the electronic band structure and the phonon dispersion of bulk *R*TeCl, the *ZT* values as a function of carrier concentration, and S, κ, and κ_e expressed as functions of the vector tensor K_n, $\tau_i(k)$, and energy eigenvalue $\varepsilon_i(k)$, which includes Refs. [73–75].

[51] M. Born, K. Huang, and M. Lax, Dynamical theory of crystal lattices, Am. J. Phys. **23**, 474 (1955).

[52] F. Mouhat and F. M. C.-X. Coudert, Necessary and sufficient elastic stability conditions in various crystal systems, Phys. Rev. B **90**, 224104 (2014).

[53] R. C. Andrew, R. E. Mapasha, A. M. Ukpong, and N. Chetty, Mechanical properties of graphene and boronitrene, Phys. Rev. B **85**, 125428 (2012).

[54] E. Cadelano, P. L. Palla, S. Giordano, and L. Colombo, Elastic properties of hydrogenated graphene, Phys. Rev. B **82**, 235414 (2010).

[55] J. Qiao, X. Kong, Z.-X. Hu, F. Yang, and W. Ji, High-mobility transport anisotropy and linear dichroism in few-layer black phosphorus, Nat. Commun. **5**, 4475 (2014).

[56] C. Pu, J. Yu, R. Yu, X. Tang, and D. Zhou, Hydrogenated PtP_2 monolayer: Theoretical predictions on the structure and charge carrier mobility, J. Mater. Chem. C **7**, 12231 (2019).

[57] T. Zhou, C. Zhang, H. Zhang, F. Xiu, and Z. Yang, Enhanced thermoelectric properties of the Dirac semimetal Cd_3As_2, Inorg. Chem. Front. **3**, 1637 (2016).

[58] Y. Hu, J. Hwang, Y. Lee, P. Conlin, D. G. Schlom, S. Datta, and K. Cho, First principles calculations of intrinsic mobilities in tin-based oxide semiconductors SnO, SnO_2, and Ta_2SnO_6, J. Appl. Phys. **126**, 185701 (2019).

[59] S. Schuler, J. E. Muench, A. Ruocco, O. Balci, D. van Thourhout, V. Sorianello, M. Romagnoli, T. Watanabe, Kand Taniguchi, I. Goykhman, A. C. Ferrari, and T. Mueller, High-responsivity graphene photodetectors integrated on silicon microring resonators, Nat. Commun. **12**, 3733 (2021).

[60] K. Yuan, X. Zhang, L. Li, and D. Tang, Effects of tensile strain and finite size on thermal conductivity in monolayer WSe_2, Phys. Chem. Chem. Phys. **21**, 468 (2019).

[61] S. Kumar, S. Sharma, V. Babar, and U. Schwingenschlögl, Ultralow lattice thermal conductivity in monolayer C_3N as compared to graphene, J. Mater. Chem. A **5**, 20407 (2017).

[62] S. Sharma, S. Kumar, and U. Schwingenschlögl, Arsenene and antimonene: Two-dimensional materials with high thermoelectric figures of merit, Phys. Rev. Appl. **8**, 044013 (2017).

[63] S.-D. Guo, Phonon transport in Janus monolayer MoSSe: A first-principles study, Phys. Chem. Chem. Phys. **20**, 7236 (2018).

[64] S. Ghosal, S. Chowdhury, and D. Jana, Electronic and thermal transport in novel carbon-based bilayer with tetragonal rings: A combined study using first-principles and machine learning approach, Phys. Chem. Chem. Phys. **23**, 14608 (2021).

[65] D. T. Morelli, V. Jovovic, and J. P. Heremans, Intrinsically Minimal Thermal Conductivity in Cubic I–V–VI_2 Semiconductors, Phys. Rev. Lett. **101**, 035901 (2008).

[66] B. Peng, H. Zhang, H. Shao, Y. Xu, X. Zhang, and H. Zhu, Thermal conductivity of monolayer MoS_2, $MoSe_2$, and WS_2: Interplay of mass effect, interatomic bonding and anharmonicity, RSC Adv. **6**, 5767 (2016).

[67] H. Shao, D. Ding, L. Zhang, C.-K. Dong, and H. Zhang, Thermoelectric performance in a Si allotrope with ultralow thermal conductivity: A first-principles study combining phonon-limited electronic transport calculations, Mater. Today Phys. **27**, 100756 (2022).

[68] S. Sharma and U. Schwingenschlögl, Thermoelectric response in single quintuple layer Bi_2Te_3, ACS Energy Lett. **1**, 875 (2016).

[69] Y. Zhang, X. Ke, C. Chen, J. Yang, and P. R. C. Kent, Thermodynamic properties of PbTe, PbSe, and PbS: First-principles study, Phys. Rev. B **80**, 024304 (2009).

[70] F. Q. Wang, S. Zhang, J. Yu, and Q. Wang, Thermoelectric properties of single-layered SnSe sheet, Nanoscale **7**, 15962 (2015).

[71] N. T. Hung, A. R. T. Nugraha, and R. Saito, Two-dimensional InSe as a potential thermoelectric material, Appl. Phys. Lett. **111**, 092107 (2017).

[72] H. Shangguan, L. Han, T. Zhang, R. Quhe, Q. Wang, S. Li, and P. Lu, Thermoelectric properties of two-dimensional gallium telluride, J. Electron. Mater. **48**, 5988 (2019).

[73] M. X. Chen and R. Podloucky, Electronic thermal conductivity as derived by density functional theory, Phys. Rev. B **88**, 045134 (2013).

[74] G. K. Madsen and D. J. Singh, BoltzTraP. A code for calculating band-structure dependent quantities, Comput. Phys. Commun. **175**, 67 (2006).

[75] Z. Gao, G. Liu, and J. Ren, High thermoelectric performance in two-dimensional tellurium: An ab initio study, ACS Appl. Mater. Interfaces **10**, 40702 (2018).